Stacking-dependent superstructures at stepped armchair interfaces of bilayer/trilayer graphene

Asieh S. Kazemi,[1,2] Simon Crampin,[1,2] and Adelina Ilie[1,2,a)]
[1]*Centre for Graphene Science, University of Bath, Bath BA2 7AY, United Kingdom*
[2]*Department of Physics, University of Bath, Bath BA2 7AY, United Kingdom*

(Received 2 December 2012; accepted 9 April 2013; published online 24 April 2013)

We present the first study of quantum interference patterns at a bilayer-trilayer armchair interface, for different stacking sequences. Visualization using scanning tunneling microscopy and theoretical calculations provides direct evidence that near armchair edges electron behavior is dominated by the "hard" edge, where the layer is abruptly truncated, as opposed to the "soft" edges, where layers continue across the boundary. Intervalley reflection causes universal quenching of the wavefunction with a periodicity of three C atoms, while the exact interference patterns depend on the stacking sequence and appear to be robust to disorder and chemical terminations.
 [http://dx.doi.org/10.1063/1.4802796]

Bilayer and trilayer graphenes have been recently identified as intrinsically interesting materials, with unique and distinctive properties and capabilities that are in the cases superior to that of monolayer graphene. Most fundamentally, their electronic structure and layer-dependent carrier density can be tuned by varying the layer stacking order,[1] and a tunable band gap opened under external perturbations.[2] Samples enriched in bilayer and trilayer graphenes or nanographenes can now be produced by techniques (e.g., chemical vapor deposition[3] or liquid phase exfoliation[4]) scalable to industrial quantities, making them accessible for future applications.

Quantum interference phenomena (QIP) at the edges of graphene systems[5–9] can dominate electron behaviour within nanographenes, nanoribbons, at junctions and boundaries within a continuous, poly-domain layer, redistributing the carrier density compared to within the bulk of the layers. Furthermore they are sensitive to—and can reveal the effects of—fundamental scattering processes at graphene boundaries and interfaces, relevant to transport characteristics.[8,9] If QIP at monolayer edges[5,6] and nanoribbons[7] are becoming well understood, there are few equivalent studies in bi- and trilayer graphene systems.

Here we investigate QIP at armchair edges of, and interfaces between, bilayer and trilayer systems, through theoretical calculations and scanning tunneling microscopy (STM). Studying stepped edges at bilayer-trilayer interfaces allows us to discriminate between the effect of a boundary within a layer, with a similar boundary but in an adjacent layer. In this way we understand factors that affect the electronic density in various layers at their edges, identify the associated electronic superstructures, and assess the importance of different scattering processes in their creation.

STM was performed with an Omicron LT-STM at 77 K in ultra-high vacuum (UHV) ($<3\times10^{-11}$ mbar), using mechanically cut PtIr tips. Nanographene flakes were produced by liquid phase exfoliation of natural graphite (Vein Graphite, Sri Lanka) in N-methyl-2-pyrrolidone (NMP)[10] and dispersed onto highly oriented pyrolitic graphite (HOPG). Annealing in UHV for 24 h at 900 °C removed residual NMP, leaving the inner areas of the sheets completely clean. Contaminants remained occasionally at edges. Tunneling conditions were typically $V_{bias} = 50$ mV, probing close to the Fermi level, and tunnelling current $I = 0.2$ nA. Near-symmetry of I when reversing V_{bias} indicated the Fermi level lay close to the Dirac point. HOPG was chosen as a substrate due to its reduced interaction with the overlaid nanoflakes.[11]

STM images were simulated by calculating[12] I flowing between an s-orbital on the tip-apex atom and few-layer graphene described by the π-electron tight-binding model with nearest[8] neighbour intralayer ($t = 3.0$ eV) and interlayer ($t' = 0.3$ eV) hopping between carbon atoms only approximating H-terminated systems. Images are of the topography $z(\boldsymbol{R})$, where $I(z(\boldsymbol{R});\boldsymbol{R}) = I_0$ for set-point current I_0. To study QIP at isolated edges we used the embedding method[13] to exactly describe the influence of the few-layer graphene extending to each side.[14] In selected cases agreement was established with *ab initio* Density Functional Theory (DFT) calculations.[13]

Figure 1 shows simulated STM images and their stacking dependence on the upper layer at armchair edges of, and monatomic stepped edges between, mono-, bi-, and tri-layer graphene. We label as A, B, and C layers displaced parallel to the armchair edge by 0, 1, and $2\times a/\sqrt{3}$, respectively, with $a = 2.46$ Å the graphene lattice constant, and stacking sequences given in lowest to uppermost layer order (i.e., AB has upper B layer). A few basic electronic superstructures appear, classified in Figure 1(a), and already noted on monolayer graphene[5] or graphite surfaces.[15–17] For AA-bilayer graphene, a honeycomb pattern occurs away from edges (i.e., in the "bulk"), which transforms into a *ribbon-like* superstructure[5] near an abrupt bilayer armchair edge (Figure 1(b)) or a monoatomic armchair step edge (Figure 1(c)), where the pattern is quenched on row numbers that are multiples of 3 indexed from the edge. This is similar to monolayer graphene.[5] For AB-bilayer, also in Figures 1(b) and 1(c), both edges again induce similar patterns, but in this case the[15] *inverse* $(\sqrt{3}\times\sqrt{3})R30°$ decays away from the edge into the *threefold* pattern, familiar from graphite.[18] These are also the dominant patterns for bilayer-trilayer armchair edges

a)Electronic mail: a.ilie@bath.ac.uk.

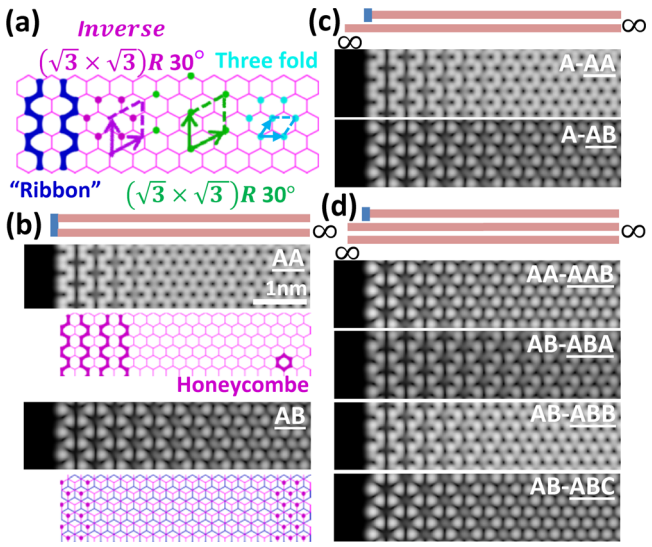

FIG. 1. (a) Taxonomy of basic electronic superstructures. (b)–(d) Simulated STM images of the top layer at armchair edges of 1, 2, and 3-layer stacks with various stacking sequences: semi-infinite top-layer(s), infinite bottom layer(s). Bilayer stacking schematics: top layer pink, bottom layer blue.

with AA-AAB and AB-ABC stacking (Figure 1(d)). For AB-ABA and AB-ABB stackings, the pattern above the trilayer appears as a weighted superposition of the above patterns. Further simulations[14] indicate little influence on the top layer pattern from the presence of a fourth layer, supporting our use of simulations on *isolated* few-layer graphene films to interpret experiments where trilayer flakes are deposited, hence unlikely to be in registry with the underlying HOPG. Finally, a $(\sqrt{3}\times\sqrt{3})R30°$ superstructure can appear in all few-layer graphenes, due to the presence of defects.[16] We will use this pattern taxonomy to analyse our experimental STM images.

Figure 2(a) shows an image recorded near an armchair edge separating bi- and trilayer regions. The stepped edge consists of a top layer recessed by ~2 nm relative to the physical boundary of the two bottom layers (see topographic profile in Figure 2(b)). We first focus on the STM pattern on the exposed bilayer region, Figure 3(a) and similarly shaped area in Figure 2(a). The *inverse* $(\sqrt{3}\times\sqrt{3})R30°$ superstructure covers much of this area, with *additional, weak intensity* present on "forbidden rows." This is the pattern noted on the AB-bilayer in Figure 1(b), although here the bilayer extends beneath a third layer beyond ~2 nm, and the bilayer edge shows evidence of a chemical edge termination (discussed below). To rationalize this behavior, we consider additional simulations of stepped interfaces between bilayer and trilayer graphene (Figure 3(b)) and bilayer nanoribbons (Figure 3(c)). The AB bilayer presents a similar near-edge pattern irrespective of whether it ends with a monatomic step down to monolayer graphene (Figure 1(c)), both layers end abruptly (Figure 1(b)), or a third, recessed, upper layer is added (Figure 3(b)): an almost identical evolution from inverse $(\sqrt{3}\times\sqrt{3})R30°$ to threefold pattern is observed. In contrast, a bilayer with a second abrupt edge, a ~2 nm wide nanoribbon, has a strongly width-dependent appearance in STM simulations which is *exclusively* inverse $(\sqrt{3}\times\sqrt{3})R30°$ (i.e., with *no intensity* on "forbidden rows") when $n = 3\times\text{integer}+2$ rows wide (which naturally accommodates the missing third row

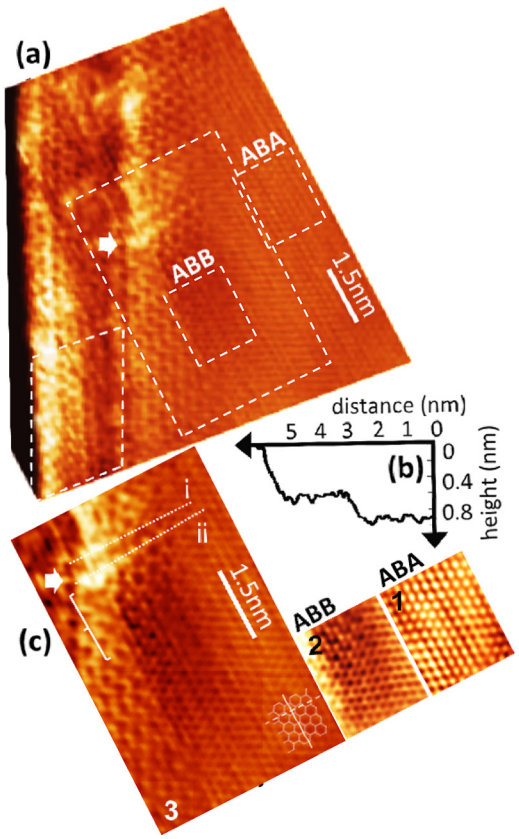

FIG. 2. (a) STM image and (b) topographic profile of bilayer-trilayer armchair boundary at an edge. Top layer reveals ABA (dominant) and ABB stackings. (c) Highlighted ABA and ABB regions, insets 1 and 2, respectively. Inset 3: ABB region in the cradle of two defective/strained regions, with lines (i) and (ii) at a non-zero angle, indicating local strain, and accolade, which marks perturbations in the edge superstructure aligned to the zigzag direction. Armchair (dashed) and zigzag (continuous) directions, in right corner.

associated with each edge) or has $(\sqrt{3}\times\sqrt{3})R30°$ character for others (Figure 3(c)). Evidently, the abrupt truncation of the layer under consideration provides the dominant influence upon electrons near the edge of the layer, acting as a "hard edge" and a strong perturbation. Much weaker effects result from the truncation of adjacent layers within the stack, which we refer to as "soft edges" below.

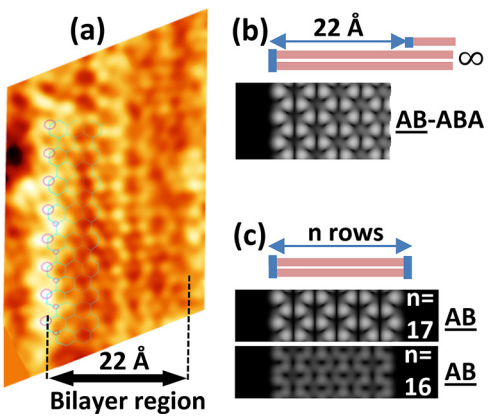

FIG. 3. (a) STM image above bilayer region at the stepped bilayer/trilayer interface corresponding to the similarly shaped area in Fig. 2(a); edge termination in purple. STM simulations of (b) edge superstructures on the bilayer side of AB-ABA bilayer/trilayer armchair interface, and (c) armchair bilayer nanoribbons $n = 17$ or $n = 16$ rows wide.

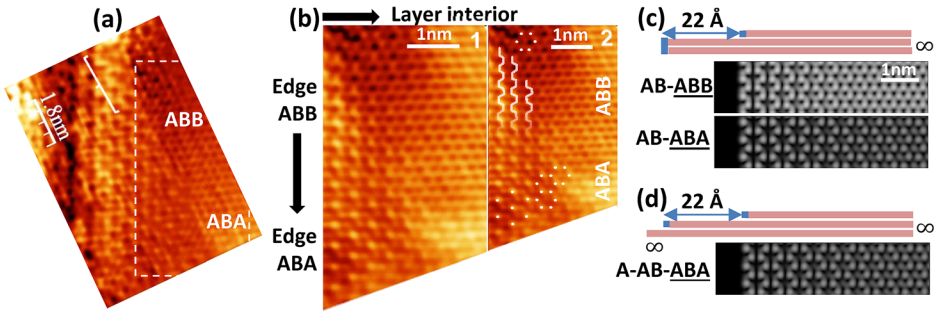

FIG. 4. (a) Experimental STM image above the top layer of the trilayer. (b) Region inside rectangle in (a) shows ABB to ABA stacking transition and change in superstructure, panel 2 highlights patterns in 1; localized edge defects produce a $(\sqrt{3}\times\sqrt{3})\,R30^\circ$ superstructure. (c),(d) Simulations: edge superstructures for different stackings and (also Fig. 1(d)) different extents of the lower layers.

The top layer of our bilayer/trilayer stack displays near-edge patterns characteristic of different stackings (Fig. 2(a)), which we identify (see below) as being predominantly ABA stacking, due to the threefold pattern (inset 1 in Fig. 2(c)) which transitions into *inverse* $(\sqrt{3}\times\sqrt{3})\,R30^\circ$ at the edge, and ABB (insets 2 and 3 in Fig. 2(c)). The precise origin of this stacking transition is unclear, but is most likely due to strain fields associated with defective/strain regions observed to align with both armchair and zigzag directions (inset 3 in Fig. 2(c)) and which gradually create the ABB region in their cradle. Notably, bright electronic features emanating from a small locality at the layer edge are in a direction (ii) inclined at a small angle relative to the original armchair direction (i). We see no evidence of extended grain boundaries such as those associated with vacancy clusters and dislocations which manifest themselves through large mis-orientation angles or armchair-to-zigzag transitions within the sheet,[19] nor of periodic, Moire-type *small-angle rotation* of layers, which have very distinctive electronic signatures.[20] Furthermore, the stacking transition is not a result of the tip lifting or/and sliding the top layer, there being no evidence of a sizeable height increase relative to the surroundings.[21]

Figure 4 highlights the patterns visible on the trilayer side of the bilayer-trilayer stepped interface and compares them with those expected for AB-ABB and AB-ABA stacking sequences. Moving from top to bottom in Figure 4(b), the characteristic ABB patterns transition into ABA features, i.e., patterns with threefold symmetry but appreciable amplitude on both sublattices of the graphene sheet transition into the *inverse* $(\sqrt{3}\times\sqrt{3})\,R30^\circ$ pattern, while closer to the edge, ribbon-like patterns become *inverse* $(\sqrt{3}\times\sqrt{3})\,R30^\circ$, in agreement with simulations shown in Figure 4(c). In the region directly at the edge (Figure 4(a)), the patterns are as expected for ABA stacking. Moreover, simulations indicate that the edge pattern on the trilayer side of the step is insensitive to the continuation of the bilayer: whether it terminates abruptly (Figure 4(c)), only the upper sheet in the bilayer terminates (Figure 4(d)), or the bilayer continues ideally (Figure 1(d)). Again the dominant edge behavior comes from the "hard edge" provided by the natural truncation of a layer and the stacking sequence.

To further discuss the STM patterns we consider the electronic structure of trilayer stacks and the effect of boundary scattering. Low energy electrons (energies close to the Dirac point) in an ABA trilayer occupy linear "monolayer-like" and parabolic "bilayer-like" bands (Figure 5(a)). Diagonalising the trilayer Hamiltonian one finds that at wave vector $\boldsymbol{K}^\xi+\boldsymbol{q}$, where Dirac point $\boldsymbol{K}^\xi=(\xi 4\pi/3a,0)$, with valley index $\xi=\pm$, states in the linear band disperse as $E=\gamma q$, where $\gamma=\sqrt{3}at/2$, and have amplitudes on sites (A1, B1, A2, B2, A3, B3) in cell n given by $\psi_{\boldsymbol{q}}^{\xi}\propto(\gamma(\xi q_x+iq_y),E,0,0,-\gamma(\xi q_x+iq_y),-E)\times e^{i(\boldsymbol{K}^\xi+\boldsymbol{q})\cdot\boldsymbol{R}_n}$, whilst for the parabolic band $E=\gamma^2q^2/\sqrt{2}t'$ and $\psi_{\boldsymbol{q}}^{\xi}\propto(\gamma(\xi q_x+iq_y),E,\sqrt{2}E,\sqrt{2}\gamma(\xi q_x-iq_y),\gamma(\xi q_x+iq_y),E)\times e^{i(\boldsymbol{K}^\xi+\boldsymbol{q})\cdot\boldsymbol{R}_n}$ (assuming $E\ll t'$). A3, B3 (A1, B1) are sublattices of the top (bottom) layer in the tri-layer stack. Thus, in the top layer, "bulk" (i.e., away from the edge) states in the linear band have equal probability on the two sites, corresponding to a honeycomb pattern as in monolayer graphene, whilst those in the quadratic band have sublattice asymmetry, $|\psi_{\boldsymbol{q}}(B3)|^2/|\psi_{\boldsymbol{q}}(A3)|^2\approx E/\sqrt{2}t'\ll 1$, resulting in a pattern in which A3 sites are more prominent—as in AB-bilayer graphene, those not directly above an atom in the layer beneath. Next, considering the respective densities of states of the two bands (Figure 5(b)), we note that far more low-energy states are associated with the parabolic band than the linear: 90% of states with energies up to 50 meV. This disparity in contribution of the bands to the tunneling current makes an overall AB-bilayer-like threefold symmetric pattern the dominant motif in STM images of bulk-like ABA-trilayer graphene, as seen in Figures 1(d), 4(c), and 4(d). States in ABB-trilayer graphene are more complex, but projecting[14] the 6×6 Hamiltonian onto the 2×2 subspace of the top layer one sees that the interaction between the topmost layer and the underlying AB-bilayer breaks the symmetry between the A3 and B3 sites and causes a greater probability of low energy electrons to be on the A3 sites, and

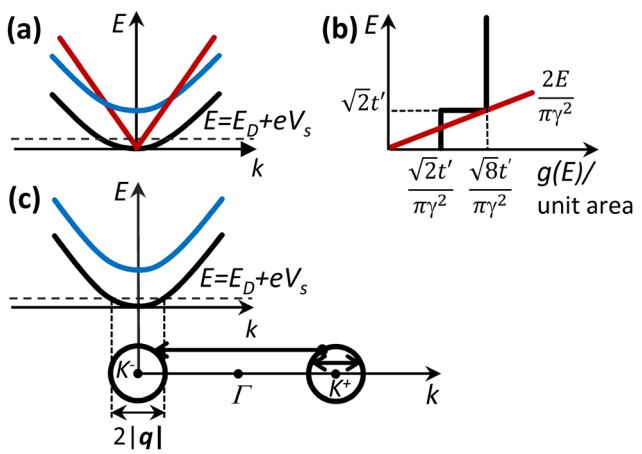

FIG. 5. ABA-trilayer graphene: (a) band structure; (b) density of states of linear and parabolic bands; (c) intervalley and intravalley scattering processes involving the dominant parabolic band. Only conduction bands shown. Dotted lines in (a), (c) symbolize the low energy levels probed here, significantly lower than $\sqrt{2}t'\approx0.2$ eV, the onset of the second set of parabolic bands.

hence again a threefold symmetric pattern in STM images (though with substantial amplitude also on the B3 sites).

At armchair edges, scattering mixes states travelling towards and away from the boundary. This has been considered for monolayer edges and monolayer-bilayer interfaces.[8] We find that in ABA trilayer, at an abrupt armchair truncation of all three layers, the state with wave vector $\boldsymbol{K}^{\pm} + (-q_x, q_y)$ is reflected into the state with wave vector $\boldsymbol{K}^{\mp} + (+q_x, q_y)$, i.e., intervalley scattering (Figure 5(c)), and that subsequent interference results in an overall wave function $\psi \propto e^{iq_y y}\sin(K^{+} \pm q_x)x$. This vanishes at $x = 0$ where the graphene sheets end, and, for small $q_x x$, on every third row of carbon atoms moving into the sheet when $x = 3 \times \text{integer} \times a/2$. The combination of this nodal pattern induced by intervalley scattering at the hard edge (reflection coefficient -1), and the intrinsic dominant threefold symmetric pattern of ABA-trilayer graphene results in the *inverse* $(\sqrt{3} \times \sqrt{3})R30^{\circ}$ motif, visible in the trilayer close to the edge in both simulated and experimental images. The superstructure decays on moving away from the edge, as de-phasing due to the varying phase difference $q_x x$ of different contributions in the energy window $[0, eV_{bias}]$ becomes increasingly important. The experimental and simulated images are actually of stepped armchair edges at bilayer/trilayer boundaries, where reflection is more complex than at a fully truncated trilayer edge, since here the wave function is only required to vanish beyond the edge on the upper layer. This opens up both transmission and *intra*-valley (Figure 5(c)) reflection scattering channels and scattering into evanescent modes associated with more distant energy bands, similar to the monolayer-bilayer boundary case.[8] With these channels active, wave functions acquire some weight on the $3 \times$ integer "forbidden" rows. However, our experimental and simulated images demonstrate that intervalley reflection remains dominant at low energies, and hence the persistence of the *inverse* $(\sqrt{3} \times \sqrt{3})R30^{\circ}$ motif in the quantum interference patterns. A similar argument leading to nodes in the wave function every three rows also holds at an armchair edge for the bilayer, where only a pair of parabolic bands exists at low energy. Our experimental STM image of the bilayer region in Figure 3(a) shows such a nodal periodicity. However, the pattern is referenced not to the bilayer edge, but approximately 2 Å inside, indicating a regular molecular termination which appears as bright features and which reflects the graphene electrons similar to a hard edge. Previous work has shown sizeable onsite potential shifts at armchair edges can influence QIP and cause a shift in the origin of the resulting superstructures;[7] here, the termination leaves the superstructure unchanged but unusually provides a non-vanishing electron density beyond the graphene lattice. Further, a degree of irregularity exists at the bilayer-trilayer stepped edge in Figures 2 and 3, yet the associated superstructures appear largely unaffected and correlate with simulations that assume ideal edges, indicating robustness to disorder in QIPs. Taken together, our analysis and previous work on monolayer graphene[7] show that the extinction of the wave function every three rows near a "hard" armchair edge is a natural consequence of the dominant inter-valley scattering that occurs at these edges and does not depend upon the number of layers in the stack nor require perfect edges.

In conclusion, we have visualised using STM and performed simulations to understand quantum interference patterns at bilayer-trilayer armchair interfaces in graphene, demonstrating the "hard" and "soft" nature of natural armchair edges for low energy electrons in sheets which terminate or continue across the boundary, respectively. The observed patterns in AB-ABA bilayer-trilayer graphene are dominated by contributions from states within the first parabolic band which result in an *inverse* $(\sqrt{3} \times \sqrt{3})R30^{\circ}$ motif close to the hard edge, while for AB-ABB stacking patterns exhibit sublattice asymmetry but with a reduced contrast compared to ABA-trilayer. Intervalley reflection produces a universal quenching of the wave function near the edge with a periodicity of three C rows, which appears robust in respect to a degree of edge disorder while specific edge terminations add complexity to the behavior of wave functions at the very edge of layers. We envisage lateral interfaces within multi-stacked graphene systems as providing unique system-specific opportunities for wave-function engineering to be exploited in devices employing quantum-interference and its impact upon transport characteristics.

This work was supported by an EPSRC Science and Innovation Award from the UK Government (Grant No. EP/G036101/1).

[1]W. Bao, L. Jing, J. Velasco, Y. Lee, G. Liu, D. Tran, B. Standley, M. Aykol, S. B. Cronin, D. Smirnov, M. Koshino, E. McCann, M. Bockrath, and C. N. Lau, Nat. Phys. **7**(12), 948 (2011); S. H. Jhang, M. F. Craciun, S. Schmidmeier, S. Tokumitsu, S. Russo, M. Yamamoto, Y. Skourski, J. Wosnitza, S. Tarucha, J. Eroms, and C. Strunk, Phys. Rev. B **84**(16), 161408 (2011); J. T. Ye, M. F. Craciun, M. Koshino, S. Russo, S. Inoue, H. T. Yuan, H. Shimotani, A. F. Morpurgo, and Y. Iwasa, Proc. Natl. Acad. Sci. U.S.A. **108**(32), 13002 (2011).
[2]Y. B. Zhang, T. T. Tang, C. Girit, Z. Hao, M. C. Martin, A. Zettl, M. F. Crommie, Y. R. Shen, and F. Wang, Nature (London) **459**(7248), 820 (2009).
[3]S. Lee, K. Lee, and Z. H. Zhong, Nano Lett. **10**(11), 4702 (2010); K. Yan, H. L. Peng, Y. Zhou, H. Li, and Z. F. Liu, *ibid.* **11**(3), 1106 (2011).
[4]C. J. Shih, A. Vijayaraghavan, R. Krishnan, R. Sharma, J. H. Han, M. H. Ham, Z. Jin, S. C. Lin, G. L. C. Paulus, N. F. Reuel, Q. H. Wang, D. Blankschtein, and M. S. Strano, Nat. Nanotechnol. **6**(7), 439 (2011).
[5]H. Yang, A. J. Mayne, M. Boucherit, G. Comtet, G. Dujardin, and Y. Kuk, Nano Lett. **10**(3), 943 (2010).
[6]C. Park, H. Yang, A. J. Mayne, G. Dujardin, S. Seo, Y. Kuk, J. Ihm, and G. Kim, Proc. Natl. Acad. Sci. U.S.A. **108**(46), 18622 (2011); J. M. Xue, J. Sanchez-Yamagishi, K. Watanabe, T. Taniguchi, P. Jarillo-Herrero, and B. J. LeRoy, Phys. Rev. Lett. **108**(1), 016801 (2012).
[7]K. Sasaki, K. Wakabayashi, and T. Enoki, J. Phys. Soc. Jpn. **80**(4), 044710 (2011).
[8]T. Nakanishi, M. Koshino, and T. Ando, Phys. Rev. B **82**(12), 125428 (2010).
[9]J. W. González, H. Santos, M. Pacheco, L. Chico, and L. Brey, Phys. Rev. B **81**(19), 195406 (2010).
[10]A. Catheline, C. Valles, C. Drummond, L. Ortolani, V. Morandi, M. Marcaccio, M. Iurlo, F. Paolucci, and A. Penicaud, Chem. Commun. **47**(19), 5470 (2011).
[11]E. Y. Andrei, G. H. Li, and X. Du, Rep. Prog. Phys. **75**(5), 056501 (2012); G. H. Li, A. Luican, and E. Y. Andrei, Phys. Rev. Lett. **102**(17), 176804 (2009).
[12]V. Meunier and P. Lambin, Phys. Rev. Lett. **81**(25), 5588 (1998).
[13]J. E. Inglesfield, Comput. Phys. Commun. **137**(1), 89 (2001).
[14]See supplementary material at http://dx.doi.org/10.1063/1.4802796 for methods describing STM simulations; graphene electronic structure for

ABA trilayer and AB bilayer, in bulk, and for scattering states at armchair edges at low energy; STM image simulations for trilayer-quadlayer vs. bilayer-trilayer stepped armchair interfaces for various stacking sequences; the effect of a soft edge; and discussion on the nature of the stacking transition.
[15]G. M. Shedd and P. E. Russell, Surf. Sci. **266**(1–3), 259 (1992).
[16]H. A. Mizes and J. S. Foster, Science **244**(4904), 559 (1989).
[17]K. Sakai, K. Takai, K. Fukui, T. Nakanishi, and T. Enoki, Phys. Rev. B **81**(23), 235417 (2010).
[18]D. Tomanek, S. G. Louie, H. J. Mamin, D. W. Abraham, R. E. Thomson, E. Ganz, and J. Clarke, Phys. Rev. B **35**(14), 7790 (1987).
[19]H. Terrones, R. Lv, M. Terrones, and M. S. Dresselhaus, Rep. Prog. Phys. **75**(6), 062501 (2012).
[20]G. T. de Laissardiere, D. Mayou, and L. Magaud, Nano Lett. **10**(3), 804 (2010); G. H. Li, A. Luican, J. M. B. L. dos Santos, A. H. C. Neto, A. Reina, J. Kong, and E. Y. Andrei, Nat. Phys. **6**(2), 109 (2010).
[21]H. S. Wong, C. Durkan, and N. Chandrasekhar, ACS Nano **3**(11), 3455 (2009).